EDGE ARTICLE

Check for updates

Ligand-mediated formation of Cu/metal oxide hybrid nanocrystals with tunable number of interfaces†

Seyedeh Behnaz Varandili, [ID] Dragos Stoian, Jan Vavra, James Pankhurst and Raffaella Buonsanti [ID] *

Combining domains of different chemical nature within the same hybrid material through the formation of heterojunctions provides the opportunity to exploit the properties of each individual component within the same nano-object; furthermore, new synergistic properties will often arise as a result of unique interface interactions. However, synthetic strategies enabling precise control over the final architecture of multicomponent objects still remain scarce for certain classes of materials. Herein, we report on the formation of Cu/MO_x (M = Ce, Zn and Zr) hybrid nanocrystals with a tunable number of interfaces between the two domains. We demonstrate that the organic ligands employed during the synthesis play a key role in regulating the final configuration. Finally, we show that the synthesized nanocrystals serve as materials platforms to investigate the impact of the Cu/metal oxide interfaces in applications by focusing on the electrochemical CO_2 reduction reaction as one representative example.

Introduction

Combining domains of different chemical nature within the same hybrid material through the formation of heterojunctions provides the opportunity to exploit the properties of each individual component within the same nano-object; furthermore, new synergistic properties will often arise as a result of unique interface interactions. In the past decade, colloidal chemistry has proven to be one of the most suitable synthetic methods to achieve tunability on hybrid materials at the nanoscale.[1–10] Indeed, colloidal hybrid nanocrystals (HNCs) have been utilized as the key components in a variety of applications spanning from catalysis to plasmonics to biomedicine and energy conversion.[1–10] Phase segregation, partial cation exchange, thermally induced coalescence and seeded growth are some of the strategies employed to access a huge library of HNCs.[1–10] Despite the beautiful examples reported in the literature, some material combinations remain more challenging or underexplored than others.

Non-noble metal/metal oxide HNCs are extremely interesting systems because of the unique synergistic interactions that arise at the interface between the two domains.[9,11,12] Nevertheless, synthetic strategies that enable precise control over the final architecture of these NCs remain scarce.[9,13–15] One of the

Laboratory of Nanochemistry for Energy (LNCE), Institute of Chemical Sciences and Engineering, École Polytechnique Fédérale de Lausanne, CH-1950 Sion, Switzerland. E-mail: raffaella.buonsanti@epfl.ch

† Electronic supplementary information (ESI) available. See DOI: 10.1039/d0sc04739b

challenges in these systems is the tendency of the non-noble metal domain to easily oxidize, which limits the reaction environment to organic solvent, and precludes the possibility of using the metal as a seed for the growth of the oxide domain, which is a common approach for HNCs.[6,16–18]

In this work, we choose Cu/CeO_2 HNCs as one example of this class of materials because of the relevance of this interface for various applications, including thermal and electrochemical CO_2 conversion.[9,19,20] We report a ligand-mediated synthesis to access $Cu/(CeO_2)_n$, with n = 1, 2, 6 representing the average number of Cu/CeO_2 heterojunctions in each particle. The CeO_2 NCs are employed as nucleation seeds for the copper and different ligands are utilized to tune the number of junctions. We demonstrate that the final architecture is crucial when seeking property tunability by providing a representative example in the electrochemical CO_2 reduction reaction. Finally, we show the generality of the synthetic concept that is applicable to construct other Cu/metal oxide heterojunctions.

Results and discussion

In a typical synthesis, 7 nm spherical CeO_2 NCs (Fig. S1†) are dispersed in octadecene (ODE) and employed as seeds. A precursor solution containing copper acetate (Cu(OAc)) and the selected organic ligands (OLAM/OLAC, OLAM/OLAC/TOP or TOP only, where OLAM = oleylamine, OLAC = oleic acid, TOP = trioctylphosphine) in ODE is injected dropwise at 300 °C into the seed solution. OLAM and OLAC are common ligands in the synthesis of HNCs including one metal oxide domain, TOP was chosen as demonstrated to play an important role in the

formation mechanism of copper NCs.[9,21] The dropwise injection was important to avoid homogeneous nucleation of copper. Various synthetic parameters (i.e. temperature, ligand concentration, amount of seeds) were optimized to maximize the yield of HNCs (i.e. $100 \times n^o$ HNCs/(n^o isolated seeds + n^o HNCs)).

Structural characterization of the (Cu/CeO$_2$)$_n$ HNCs

Fig. 1 gives an overview on the Cu/CeO$_2$ HNCs synthesized with OLAC/OLAM (Fig. 1a and b), OLAM/OLAC/TOP (Fig. 1c and d) and TOP only (Fig. 1e and f). TEM images at lower magnifications are also provided in Fig. S2† to confirm the homogeneity of the samples. The HNC yield, as measured by statistical analysis in TEM images, was 80%, 92% and 90%, meaning that less than 20%, 8% and 10% of ceria seeds remain isolated, respectively. No homogeneously nucleated Cu NCs are identified. Representative X-ray diffraction (XRD) patterns of the HNCs are reported in Fig. S3.†

Transmission electron microscopy (TEM), high-angle annular dark-field scanning TEM (HAADF-STEM) and the relative area-selective energy-dispersive X-ray spectroscopy (EDXS) maps evidence the systematic formation of HNCs consisting of one central domain of spherical Cu, with an average size of around 15 nm, and one or more CeO$_2$ domain seeds of around 7 nm. For the rest of the manuscript, these HNCs will be referred to as Cu/(CeO$_2$)$_n$ with $n = 1,2,6$ indicating the average number of heterojunctions in each NCs based on a statistical analysis of the stoichiometry distribution (Fig. 2). Concomitantly, elemental analysis performed by inductively coupled plasma-optical emission spectroscopy (ICP-OES) indicates decreasing Cu : Ce ratio as n increases (3.6 : 1, 2.1 : 1 and 1.7 : 1 for Cu/(CeO$_2$)$_1$, Cu/(CeO$_2$)$_2$ and Cu/(CeO$_2$)$_6$, respectively).

Fig. 2 Statistical analysis of the number of hetero-junctions in: (a) Cu/(CeO$_2$)$_2$ and (b) Cu/(CeO$_2$)$_6$. This analysis was performed by counting at least 100 HNCs per sample.

Clearly, the number of the ceria domains in each hybrid architecture depends on the employed ligand mixture. Specifically, OLAC/OLAM (Fig. 1a and b), OLAM/OLAC/TOP (Fig. 1c and d) and TOP only (Fig. 1e and f) lead to the formation of Cu/(CeO$_2$)$_1$, Cu/(CeO$_2$)$_2$ and Cu/(CeO$_2$)$_6$, respectively.

High-resolution TEM was performed to investigate the nature of the interface. Notably, the samples were ultrasonicated immediately before deposition on the grid as a proof that the two domains are permanently linked in one object. Fig. 3 shows that the Cu and CeO$_2$ NCs are intimately connected, however no straightforward epitaxial relationship was observed, which is reasonable considering the high misfit between the lattice parameters of Cu and CeO$_2$. X-Ray photoelectron spectroscopy (XPS) analysis provides an additional proof that the two domains are coupled as the electronic structure of the HNCs is different than the physical mixture of Cu and CeO$_2$ NCs (Fig. S4†).

Investigation of the role of the ligands

Configurations of HNCs similar to Cu/(CeO$_2$)$_2$ and Cu/(CeO$_2$)$_6$ have been previously reported in the literature and were often referred to as flower- or clover-like structures.[3,6,16,17,22–25] However, in these examples, the HNC core always consists of the NC seeds. Oppositely, in Cu/(CeO$_2$)$_2$ and Cu/(CeO$_2$)$_6$, the core is the nucleating Cu domain while the "petals" are the ceria seeds, which is both unique and surprising. As for the

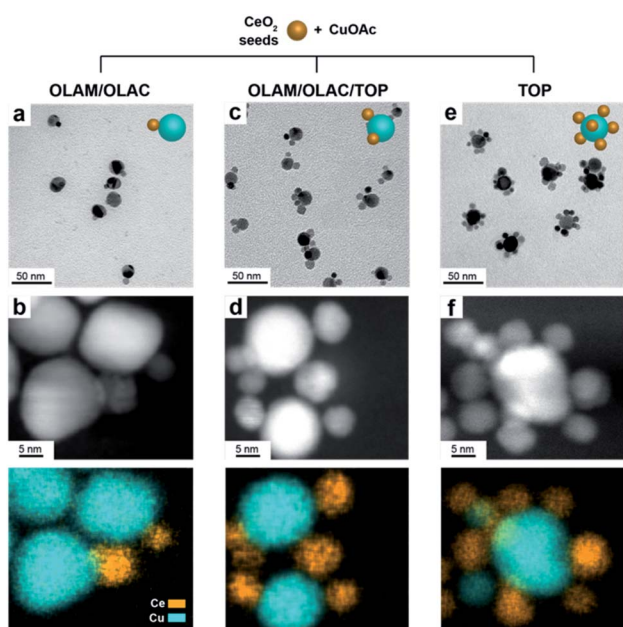Fig. 1 (a, c, e) Representative TEM and (b,d,f) HAADF-STEM images and corresponding EDXS elemental maps of (a, b) Cu/(CeO$_2$)$_1$, (c, d) Cu/(CeO$_2$)$_2$ and (e,f) Cu/(CeO$_2$)$_6$, synthesized in the presence of OLAC/OLAM, OLAC/OLAM/TOP and TOP only, respectively.
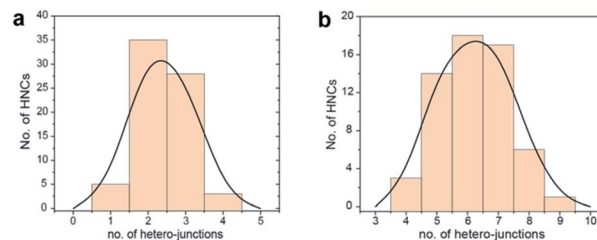

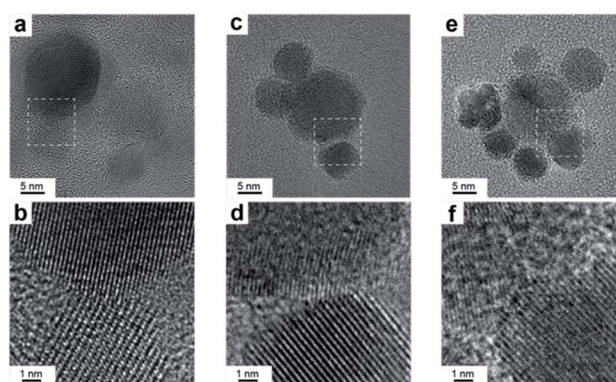
Fig. 3 HR-TEM characterization of: the HNCs (a, c, e) and the interface areas shown by white squares (b, d, e) for (a, b) Cu/(CeO$_2$)$_1$, (c, d) Cu/(CeO$_2$)$_2$ and (e, f) Cu/(CeO$_2$)$_6$, synthesized in the presence of OLAC/OLAM, OLAC/OLAM/TOP and TOP only, respectively.

mechanism, the formation of abovementioned flower- or clover-like structures has been correlated to the polarity of the solvent, the change of seed size or structure (single crystal *vs.* multi-twinned) and the reaction time.[3,6,16,17,22–25] In our system, the solvent and the seeds are the same for all of the HNCs so their influence on the heterojunction formation can be ruled out. Instead, the chemical nature of the ligands clearly plays a significant role.

Ligands can impact NC nucleation and growth in two main ways: by modulating the surface chemistry and by acting as reactants in the synthesis (*i.e.* complexing agents or reductants).[2,26]

From the results above, it is clear that the presence of TOP in the reaction mixture induces the formation of multiple heterojunctions. Interestingly, no convincing evidence of the TOP acting as surface ligand on Cu/(CeO$_2$)$_2$ and Cu/(CeO$_2$)$_6$ HNCs was found by Fourier transform infrared spectroscopy (FT-IR) and XPS (Fig. S5†). Another possibility is that TOP alters the surface chemistry of the seeds by exchanging with the original OLAM ligand of the CeO$_2$ NC seeds during the synthesis. However, no HNCs formed when TOP-coated CeO$_2$ NCs were used as seeds in place of the OLAM-coated ones; instead, only homogeneous nucleation of Cu NCs occurred (Fig. S6†). These results suggest that TOP plays a key role as complexing agent for the formation of petal-like HNCs and must be involved in the Cu monomer formation as previously observed.[21]

Fig. 4 reports the NMR spectra of the precursor solutions (CuOAc + TOP) and (CuOAc + OLAM/OLAC). The data for the (CuOAc + TOP) mixture (Fig. 4a) indicate the formation of a [Cu(TOP)$_4$][OAc] complex, where the acetate anion is non-coordinating. In the ^{31}P{^{1}H} NMR spectrum, the large shift of the free TOP signal to a more positive chemical shift, as well as

the broadening of the resonance, are strong indicators of coordination to the Cu$^+$ center.

All four coordinated TOP molecules are clearly symmetry equivalent, indicating a tetrahedral geometry. Likewise, in the ^{1}H NMR spectrum, the free TOP alpha- and beta-CH$_2$ resonances move to more positive chemical shift values after coordination to Cu$^+$, and are also broadened due to the quadrupolar moment on Cu. A resonance for the OAc ligand was also observed, and its integration indicates the expected 1 : 4 ratio with TOP. No free TOP is observed in the precursor mixture.

In the case of the (CuOAc + OLAM/OLAC) mixture (Fig. 4b), there are a number of broad resonances in the ^{1}H NMR spectrum that can be assigned to the α- and β-CH$_2$ environments of either OLAM and/or OLAC. In a control experiment, OLAM and OLAC were mixed and the ^{1}H NMR spectrum was measured; the spectrum was consistent with an oleylammonium oleate salt, which forms from the acid–base reaction between OLAM and OLAC, as expected. The ^{1}H NMR spectrum of the precursor mixture compared quite well with this spectrum, albeit with an important difference: the well-resolved resonances for the α-CH$_2$ protons in the [OLAM-H][OLAC] salt (2.67 and 2.36 ppm) appear as a single broad resonance in the precursor mixture (2.44 ppm). An equivalent observation was made for the β-CH$_2$ protons (peaks at 1.78 and 1.62 ppm averaging to 1.74 ppm). This loss of resolution could be due to association of the ammonium carboxylate ions with Cu$^+$. The speciation of copper ions in ionic solutions has previously been shown to be quite complex, where transition metals tend to coordinate to additional anions, forming anionic complexes.[27] These complexes are then surrounded by associated cations, in mono- or multi-nuclear aggregates.[28] We therefore tentatively propose that Cu$^+$ is coordinated by four oleate ligands in a tetrahedral geometry, with three oleylammonium counter ions balancing the charge, *i.e.* [Cu(OLAC)$_4$][(OLAM-H)$_3$].

Fig. 4 Characterization of the precursor solutions. (a) ^{31}P{^{1}H} NMR spectra and ^{1}H NMR spectra of the Cu complex formed by a combination of CuOAc and TOP. (b) ^{1}H NMR spectra of the Cu complex formed by a combination of CuOAc, OLAM and OLAC. The proposed molecular structures of the Cu complexes in each mixture are shown on the right of the corresponding spectra.

Discussion on the formation mechanism of the HNCs

Generally, two different mechanisms might take place to form the HNCs: an aggregative electrostatic self-assembly and heterogeneous nucleation. In the former, the Cu NCs would homogeneously self-nucleate in solution and successively assemble with the CeO$_2$ seeds. Here, the ligands would modulate the surface passivation and charge to drive such a controlled attachment. In the heterogeneous nucleation, the CeO$_2$ NCs would act as seeds for the nucleation of the Cu domain.

To get further insights, we monitored the temporal evolution for Cu/(CeO$_2$)$_1$ (Fig. S7†) and Cu/(CeO$_2$)$_6$ (Fig. 5). In both cases, the TEM analysis suggests that the configuration of the HNCs, with either single or multiple heterojunctions, is established since the early stages of the synthesis and an increased reaction time contributes towards the growth of the Cu domains (Fig. 5a–c). No evidence of homogeneously nucleated Cu NCs was found at any time. As for the CeO$_2$ seeds, statistical analysis on the TEM images indicates a sudden drop of isolated NCs at around 75 s (Fig. 5d), which corresponds to the time at which the HNCs are first observed in the TEM images. In order to
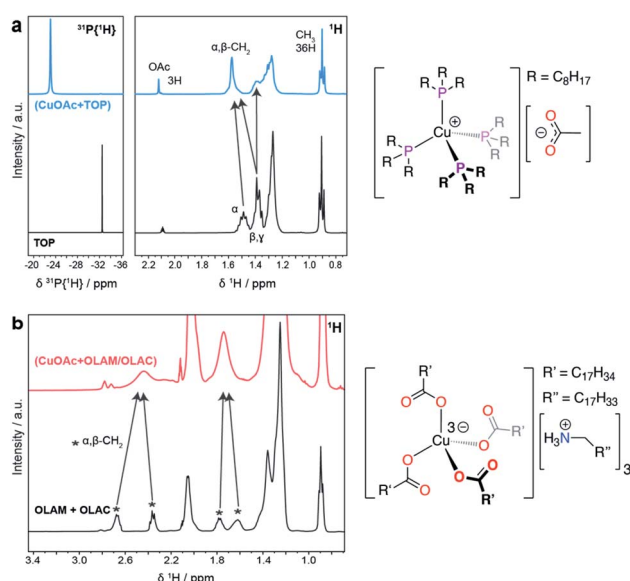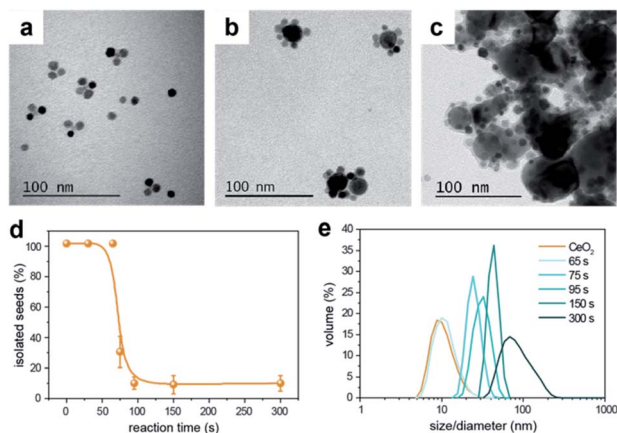
Fig. 5 Temporal evolution of the HNCs. (a, b, c) Representative TEM images of samples collected at a reaction time of (a) 75 s, (b) 150 s and (c) 300 s; (d) percentage of isolated CeO_2 seeds versus the reaction time obtained from statistical analysis on TEM aliquots; (e) DLS spectra of aliquots collected at different reaction times. All data are relative to the synthesis of $Cu/(CeO_2)_6$.

Fig. 6 Schematic representation of the proposed pathway toward the formation of different $(Cu/CeO_2)_n$ HNCs.

exclude the impact of aggregation during drying of the TEM grid, dynamic light scattering (DLS) was performed as a complementary technique (Fig. 5e). Consistently with the TEM data, a continuous increase of particle size in solution is observed, which tracks well the increase in the Cu domain size. If aggregative growth of the HNCs occurred, a bimodal distribution should have been detected at some point, which was not the case. Therefore, as far as the current experimental evidences indicate, heterogeneous nucleation is the main mechanism behind the formation of the HNCs.

If heterogeneous seeded-growth is taking place, then the nature of the complexes formed between the ligands and the Cu precursor must play a role in determining the final configuration of the HNCs. Based on the metal–ligand bond strengths and on previous calculations,[21] the copper–phosphine complex is expected to be more stable than the copper complex forming in the OLAM/OLAC mixture, and so to decompose more slowly and/or only at high temperature to release the copper monomers in solution. As a matter of fact, when the two precursor solutions were left at room temperature for two days and monitored via UV-vis spectroscopy (Fig. S8†), the (CuOAc + OLAM/OLAC) mixture turned blue and a brown sediment was observed at the bottom of the vial; instead, no change was observed in the (CuOAc + TOP), in agreement with its higher redox stability. Furthermore, when the reaction temperature was decreased from 300 °C to 270 °C (Fig. S9†), neither HNCs or Cu NCs formed when utilizing (CuOAc + TOP), instead Cu/CeO_2 HNCs were detected when (CuOAc + OLAM/OLAC) was employed. The above experimental evidences suggest that the organic ligands can regulate the copper monomer supersaturation by modulating the precursor stability. Specifically, we speculate that (CuOAc + TOP) and (CuOAc + OLAM/OLAC) result in low and high supersaturation, respectively, when they are delivered to the seed-containing reaction mixture. Low supersaturation is expected to induce a kinetic preference for high-
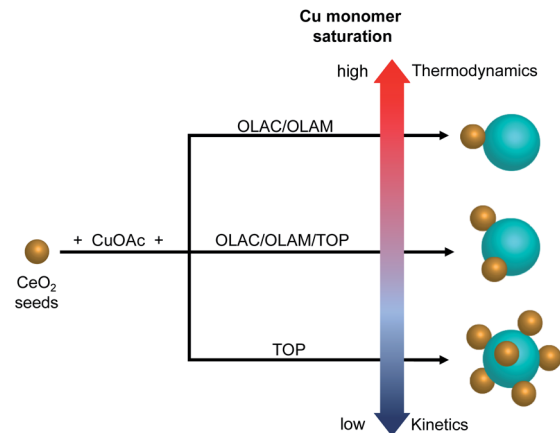
energy products.[2] In the HNCs, a significant lattice mismatch exists between ceria ($a = b = c = 5.411$ Å) and copper ($a = b = c = 3.610$ Å), and so the system will tend to minimize the free energy by reducing the number of interfaces between the two domains. Therefore, $Cu/(CeO_2)_1$ form, through the formation of a partially amorphous interface, when the OLAM/OLAC mixture is employed during the synthesis. Instead, the multi-junction HNCs, $Cu/(CeO_2)_2$ and $Cu/(CeO_2)_6$, are obtained when TOP is used instead.

Overall, the absence of isolated Cu domains at any time during the synthesis along with no TOP on the surface of the HNCs and instead involved in the formation of Cu-TOP, suggest that electrostatic self-assembly is unlikely. While still speculative at this time, the ligand-regulated monomer saturation offers an alternative explanation to the undoubted role played by the ligands in determining the number of heterojunctions in the HNCs (Fig. 6).

Impact of the number of heterojunctions on CO_2 reduction reaction (CO_2RR)

To illustrate the importance of controlling the number of heterojunctions in the HNCs, the performance of the $(Cu/CeO_2)_n$ hybrids as electro-catalysts for CO_2RR were investigated. In a previous study, we found the Cu/CeO_2 interface to promote CO_2RR versus the competing hydrogen evolution reaction (HER) and to form methane as the major CO_2RR product.[9] Operando X-ray absorption spectroscopy (XAS) and DFT calculations explained this behavior based on the promotion of the $Ce^{4+} \rightarrow Ce^{3+}$ reduction and the concomitant formation of oxygen vacancies. The latter accounts for improved stabilization of the key CO_2RR intermediates (CHO^* and H_2CO^*) at the Cu/CeO_2 interface.[9] Based on these results, understanding if an increased interfacial area further enhances these beneficial effects is interesting and crucial to develop better catalysts.

Fig. 7a reports the faradaic efficiencies (FE) and CO_2RR partial current densities (J_{CO2RR}) normalized by the electrochemically active surface area (ECSA-Fig. S10†) for Cu–CeO_2 physical mixture, $Cu/(CeO_2)_1$, $Cu/(CeO_2)_2$, and $Cu/(CeO_2)_6$
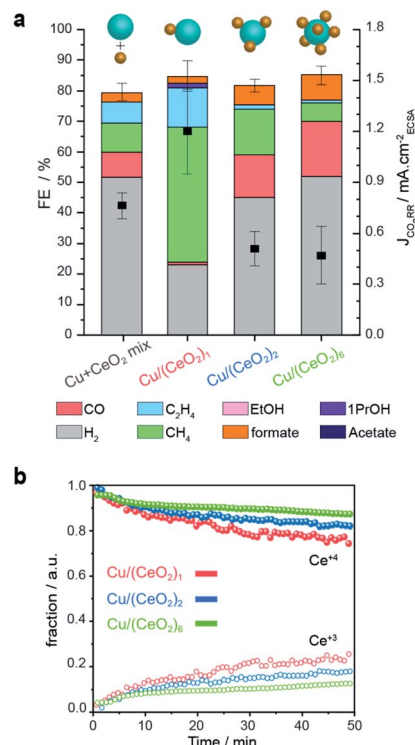
Fig. 7 CO_2RR performance of the Cu/$(CeO_2)_n$ HNCs. (a) faradaic efficiencies and CO_2RR partial current-densities for Cu/$(CeO_2)_1$, Cu/$(CeO_2)_2$ and Cu/$(CeO_2)_6$ and Cu–CeO_2 physical mixture measured at -1.2 V_{RHE} in 0.1 M $KHCO_3$. It is worth mentioning that the total FE of the samples are less than 90%. Oxidation of some unaccounted formate and methanol at the platinum anode has been reported to contribute to the lack of 100% total FE.[29,30] Also, some electrons may be used for the formation of oxygen vacancies in CeO_{2-x}, thus, contributing to non-productive current.[9] (b) Concentration profiles of Ce^{4+} (solid symbols) and Ce^{3+} (open symbols) derived from the multivariate analysis of Ce L_3-edge XANES spectra during CO_2RR.

HNCs, respectively. Data for isolated Cu and CeO_2 NCs of similar sizes of the HNC domains are reported in Fig. S11† for reference. First of all, the results evidence that the Cu/$(CeO_2)_1$ HNCs outperform the isolated Cu NCs and Cu–CeO_2 physical mixture in terms of total FE towards CO_2RR, which reaches up to 60%. The higher J_{CO2RR} indicates that such increase in FE is related to the higher intrinsic activity of the HNCs. In agreement with our previous study, Cu/$(CeO_2)_1$ produce methane as the major product with FE up to 50%.[9] This result highlights the role of the hetero-junction obtained by employing the colloidal synthesis method presented herein. Notably, as the number of heterojunctions increases, the CO_2RR FE decreases to around 37% and 32% for Cu/$(CeO_2)_2$ and Cu/$(CeO_2)_6$, respectively. Among the CO_2RR products, both ethylene and methane are suppressed while CO and formate are promoted. Concomitantly, the J_{CO2RR} is lower for the two samples compared to the single junction HNCs. Overall the FEs for CO_2RR of Cu/$(CeO_2)_{n\geq2}$ HNCs are comparable to the isolated Cu NCs (Fig. S11†), however the ratio of C_1/C_2 products is increased which could be an indication of interrupted pathway toward C_2 products. The lower J_{CO2RR} indicates that the overall intrinsic activity towards CO_2RR decreases as well.

To gain further insight into the oxidation states of the Cu and Ce domains during CO_2RR, we performed *operando* XAS measurements. Fig. 7b shows the concentration profiles of Ce^{4+} (solid symbols) and Ce^{3+} (open symbols) as a function of the reaction time at the operating potential. These values were extracted from a time-resolved map *via* multivariate spectral analysis (Fig. S12†). In all three samples, we observed the reduction $Ce^{4+} \rightarrow Ce^{3+}$ over time until reaching a steady state value. Instead, the Cu counterpart, partially oxidized at the beginning of the experiment, reduced very quickly and at a similar rate in all the samples as soon as the negative operating potential was applied; then, it remained stable in its metallic form during the catalysis (Fig. S12†). Importantly, we found that a larger fraction of Ce^{3+} forms in the Cu/$(CeO_2)_1$ HNCs compared to the Cu/$(CeO_2)_{n\geq2}$ HNCs (roughly 25% > 15% > 10% as n increases from 1 to 6). Thus, the results from the *operando* XAS of Ce L_3-edge confirm the positive correlation between Ce^{3+} and the CO_2RR promotion. They also suggest that the presence of multiple metal oxides surrounding the Cu NCs inhibits the $Ce^{4+} \rightarrow Ce^{3+}$ transformation, which is opposite to what expected based on increased interfacial area. One possible explanation is that, as the number of heterojunctions increases, the constant number of the charges (supplied from applied negative potential, -1.2 V_{RHE}) have to be distributed among a higher number of ceria NCs. As the loading and size of the Cu NCs in all the samples are constant, it's reasonable that the charge portion allotted to each ceria NCs would decrease.

Moreover, one must consider that increasing the number of ceria domains reduces the copper surface available to perform CO_2RR. The CeO_2 NCs themselves are mostly active for HER (Fig. S11†), therefore we hypothesize that the increased HER results from their increase weight fraction in the catalyst. As the protons are consumed by the ceria, less remain available for the proton coupling steps needed to convert CO to higher hydrocarbons. Thus, mostly CO increases among the CO_2RR products while CH_4 and C_2H_4 decrease. More detailed studies are planned for the future to further corroborate this hypothesis. For example, HNCs with a reverse configuration where the several Cu NCs nucleated on one CeO_2 seed, would be an interesting system to study as the number of heterojunctions will increase without compromising the Cu surface available for the CO_2RR to take place.

Generality of the synthetic method

Finally, having learned the crucial role of the organic ligands in controlling the number of heterojunctions in the Cu/CeO_2 HNCs, we decided to investigate if the same synthesis approach could be applied to different systems. We selected ZrO_2 and ZnO as examples, because Cu/ZrO_2 and Cu/ZnO interfaces are of potential interest for both CO_2 hydrogenation and CO_2RR.[31,32] Fig. 8 depicts the Cu/ZnO (Fig. 8a–c) and Cu/ZrO_2 (Fig. 8d–f) HNCs that were successfully obtained with a configuration resembling that of Cu/CeO_2, where the central copper domain is decorated by a number of metal oxide seeds, and with the number of heterojunctions increasing as OLAM/OLAC, OLAM/OLAC/TOP or TOP only were used as the organic ligands
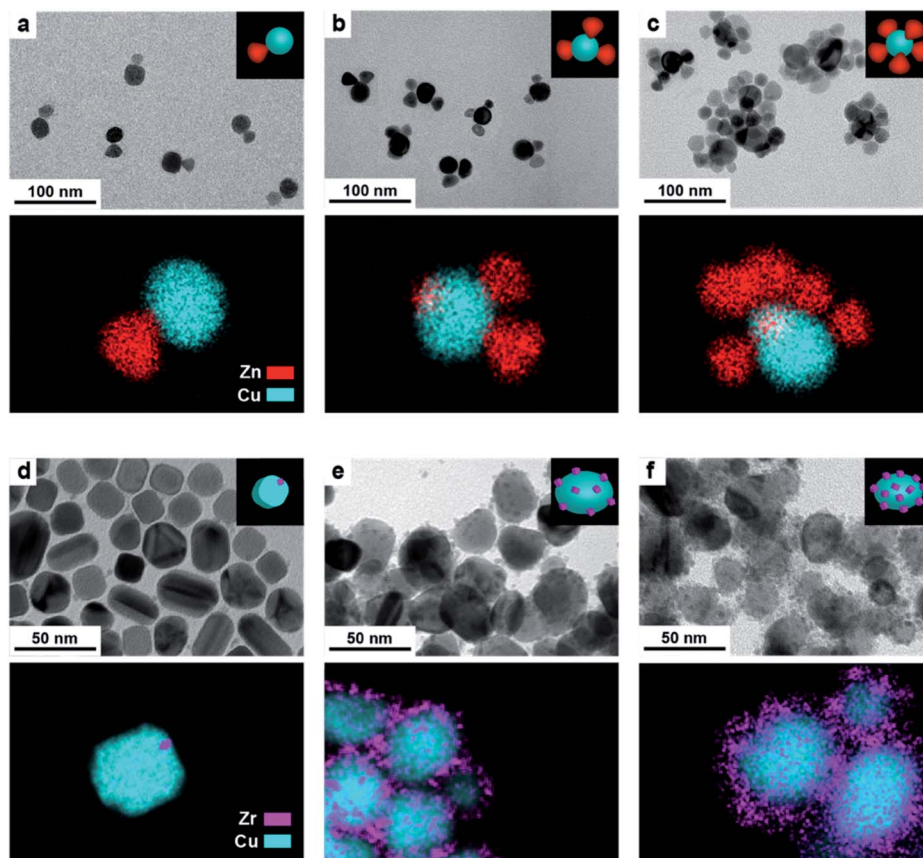
Fig. 8 Generality of the synthetic approach. TEM images and corresponding EDXS elemental maps of Cu/ZnO HNCs (a–c) and Cu/ZrO$_2$ HNCs (d–f) synthesized using (a, d) OLAM/OLAC, (b, e) OLAM/OLAC/TOP and (c, f) TOP only.

during the synthesis. While some system specific differences emerge in the final HNCs (*i.e.* the faceted morphology of the Cu domain in Fig. 8d, which might stem from some effects induced by the crystallinity of ZrO$_2$ seeds[3,6,16,17,22–25,33,34]), the results suggest that the method is indeed general.

Conclusions

In summary, we have successfully developed a seeded-growth approach to synthesize Cu/metal oxide HNCs with adjustable numbers of interfaces. Investigating the role of the ligands was key to understand that they affect the copper precursor stability and, thus, the monomer saturation, which in turn governs the growth regime and the final configuration of the HNCs. Finally, we also demonstrate that the achieved degree of architectural tunability is crucial to explore synergistic interface effects in catalysis. By testing Cu/(CeO$_2$)$_n$ as electrocatalysts for CO$_2$RR, we learned that optimal electrocatalytic properties are obtained as a trade-off between interfacial synergy and geometric configuration determining accessibility of the catalytic surfaces.

Having tunable materials platforms, like the (Cu/CeO$_2$)$_n$ HNCs reported in this study, becomes crucial to enable these correlations in catalysis and in other applications where these interfaces might be useful, such as plasmonic, biomedical, sensing and photocatalysis applications.[3,31,32,35–37] Therefore,

additional efforts in the community to understand the chemistry behind the formation of such tailored structures are important to further master the synthesis of other non-noble metal/metal oxide HNCs.

Experimental section

Chemicals

Copper(I) acetate (or CuOAc, 97%), trioctylphosphine ({CH$_3$(CH$_2$)$_7$}$_3$P, or TOP, 90%), oleic acid (C$_{17}$H$_{33}$CO$_2$H or OLAC, 90%), oleylamine (C$_{17}$H$_{33}$NH$_2$ or OLAM, 70%), 1-octadecene (C$_{18}$H$_{36}$ or ODE, 90%) were all purchased from Sigma-Aldrich and used as received.

Synthesis

Synthesis of Cu/(MO$_x$)$_1$ HNCs (M = Ce, Zn, Zr). As a general procedure, 30 mL of the ODE solution containing the MO$_x$ seeds (0.5 mM) in a 100 mL three-necked flask were degassed under dynamic vacuum for 20 min at 130 °C, after which they were heated under N$_2$ flow to 300 °C for 5 minutes. A precursor solution was prepared by mixing 0.1 mmol CuOAc and 0.4 mmol of OLAM/OLAC in degassed ODE (1.4 mL). 450 µL of this solution were then added dropwise to the flask containing the seeds at a rate of 0.18 mL min^{-1} using a syringe pump, meanwhile the reaction mixture slowly turned from colorless to

brown. At the end of the injection, after around 150 s, the reaction was stopped and the mixture was allowed to cool down to room temperature by removing the heating mantle. The HNCs were extracted and purified by repeated washing/centrifugation cycles inside a N_2 glovebox to avoid Cu oxidation. 30 mL each of anhydrous ethanol and toluene were added to the reaction mixture at room temperature and the mixture was divided into 4 centrifugation vials; the particles were collected by centrifugation at 5000 rpm for 15 min. The precipitate was washed twice with ethanol to remove unreacted precursor and surfactants. Finally, the HNCs were re-dispersed in hexane or toluene.

Synthesis of $Cu/(MO_x)_2$ HNCs (M = Ce, Zn, Zr). The same procedure was used as for the synthesis of $Cu/(MO_x)_1$ HNCs except the precursor solution contained 0.1 mmol of CuOAc, 0.396 mmol of TOP, 0.02 mmol of OLAM and 0.02 mmol of OLAC.

Synthesis of $Cu/(MO_x)_6$ HNCs (M = Ce, Zn, Zr). The same procedure was used as for the synthesis of $Cu/(MO_x)_1$ HNCs except the precursor solution contained 0.1 mmol of CuOAc and 0.4 mmol TOP.

Characterization

Electron microscopy. Samples were drop-cast on a copper TEM grid (Ted Pella, Inc.) prior to imaging. BF-TEM images were taken with a FEI Tecnai Spirit at 120 keV. HAADF-STEM imaging and energy dispersive X-ray analysis (EDX) were performed on a FEI Tecnai Osiris transmission electron microscope in scanning mode at an accelerating voltage of 200 kV. This microscope is equipped with a high brightness X-FEG gun, silicon drift Super-X EDX detectors and a Bruker Esprit acquisition software. Aberration-corrected (Cs) high-resolution S/TEM imaging were performed on a FEI Titan Themis 60–300 at an accelerating voltage of 200 kV.

Nuclear magnetic resonance (NMR). All NMR spectra were recorded on a Bruker AVANCE III HD 400 spectrometer fitted with a 5 mm BBFOz probe, operating at 400.13 MHz for ^{1}H NMR spectra and 161.98 MHz for ^{31}P{^{1}H} NMR spectra. ^{1}H NMR chemical shifts were referenced internally to residual solvent resonances (d_6-benzene, $\delta_H = 7.16$ ppm; d_8-toluene, $\delta_H = 7.09$ ppm), calibrated against an external standard ($SiMe_4$, where $\delta_H = 0$ ppm).

Dynamic light scattering (DLS). DLS spectra were collected on a Brookhaven Zeta instrument. Aliquots were extracted from the reaction mixture at different times and diluted in toluene. The DLS cell was sealed under N_2 or ambient atmosphere during the whole test period.

Inductively coupled plasma-optical emission spectrometry (ICP-OES). ICP-OES was performed on Agilent 5100 model to determine the Ce and Cu concentration in Cu/CeO_2 NCs, Cu-CeO_2 physical mixture and individual Cu NCs. For the digestion of the solutions, upon evaporation of the hexane, 280 μL of each HNO_3 (70%) and H_2O_2 (35%) was added to 100 μL of the as-synthesized NCs solutions and left overnight to ensure complete digestion of the samples. Following this step, 9.5 mL of Milli-Q water was added to the solution to reach the 2% acid

content needed for the analysis. 5 standard solutions of Ce and Cu were prepared to obtain the calibration curve that was used to determine the concentrations of the digested solutions.

Electrocatalytic measurements

Electrode preparation. Glassy-carbon plate electrodes (Type 2, Alfa Aesar, 2.5 cm × 2.5 cm) were used as substrates. They were polished using Milli-Q water slurries of 1 μm diamond (Bioanalytical Systems, Inc.) and 50 nm gamma alumina (Bioanalytical Systems, Inc.) on polishing pads. The plates were rinsed with Milli-Q water, sonicated in Milli-Q water for 10 minutes, and blown dry with nitrogen. The NCs were drop-casted on the substrate from their toluene suspension with a Cu mass loading of 15 μg for all the samples.

Electrocatalytic measurements. The electrocatalytic measurements were performed in a conventional H-cell, used in previous work by our group and by others.[9]

A Biologic SP-300 was used as the potentiostat. Platinum foil was employed as the counter electrode and an Ag/AgCl reference electrode (leak free series from Innovative Instruments, Inc.) was used. Voltages were converted to the reversible hydrogen electrode (RHE) scale.

For gas product analysis, a gas chromatograph (GC, SRI instruments) equipped with a HayeSep D porous polymer column, thermal conductivity detector, and flame ionization detector was used. Ultrahigh purity N_2 (99.999%) was used as a carrier gas. After passing through the cell, CO_2 was flowed directly into the gas-sampling loop of the GC for online gaseous product analysis, which was carried out every 10 min. For all experiments, electrolysis was carried out for 80 min with gas analysis recorded at 10 min intervals. The liquid products were collected from the electrolyte after electrolysis and analyzed by the high-performance liquid chromatography (HPLC) on an UltiMate 3000 instrument from Thermo Scientific.

Operando X-ray absorption spectroscopy (XAS)

Operando XAS experiments were performed at the SuperXAS beamline at the Swiss Light Source synchrotron facility (Paul Scherrer Institute, Switzerland). The measurements were performed in fluorescence mode at an incident angle of about 45 degrees.

We employed a dedicated set-up for the low energy Ce L_3-edge as described in our previous work.[9] The catalyst solution was drop-casted on a thin (2.5 × 2.5 × 0.5 mm^3) glassy carbon (GC) support and a Kapton window allows the X-rays to pass through. Additional details for the data analysis are reported in the ESI.†

Conflicts of interest

There are no conflicts to declare.

Acknowledgements

Notes and references

1 J. L. Fenton, B. C. Steimle and R. E. Schaak, *Science*, 2018, **360**, 513–517.

2 A. N. Chen, M. M. Scanlan and S. E. Skrabalak, *ACS Nano*, 2017, **11**, 12624–12631.

3 S. Peng, C. Lei, Y. Ren, R. E. Cook and Y. Sun, *Angew. Chem., Int. Ed.*, 2011, **50**, 3158–3163.

4 L. Amirav, F. Oba, S. Aloni and A. P. Alivisatos, *Angew. Chem., Int. Ed.*, 2015, **54**, 7007–7011.

5 U. Banin, Y. Ben-Shahar and K. Vinokurov, *Chem. Mater.*, 2014, **26**, 97–110.

6 J. Piella, A. Gónzalez-Febles, J. Patarroyo, J. Arbiol, N. G. Bastús and V. Puntes, *Chem. Mater.*, 2019, **31**, 7922–7932.

7 S. Najafishirtari, C. Guglieri, S. Marras, A. Scarpellini, R. Brescia, M. Prato, G. Righi, A. Franchini, R. Magri, L. Manna and M. Colombo, *Appl. Catal., B.*, 2018, **237**, 753–762.

8 M. Cargnello, *Chem. Mater.*, 2019, **31**, 576–596.

9 S. B. Varandili, J. Huang, E. Oveisi, G. L. De Gregorio, M. Mensi, M. Strach, J. Vavra, C. Gadiyar, A. Bhowmik and R. Buonsanti, *ACS Catal.*, 2019, **9**, 5035–5046.

10 A. Aitbekova, E. D. Goodman, L. Wu, A. Boubnov, A. S. Hoffman, A. Genc, H. Cheng, L. Casalena, S. R. Bare and M. Cargnello, *Angew. Chem.*, 2019, **131**, 17612–17618.

11 M. Cargnello, V. V. T. Doan-Nguyen, T. R. Gordon, R. E. Diaz, E. A. Stach, R. J. Gorte, P. Fornasiero and C. B. Murray, *Science*, 2013, **341**, 771–773.

12 T. W. van Deelen, C. Hernández Mejía and K. P. de Jong, *Nat. Catal.*, 2019, **2**, 955–970.

13 M. Casavola, A. Falqui, M. A. García, M. García-Hernández, C. Giannini, R. Cingolani and P. D. Cozzoli, *Nano Lett.*, 2009, **9**, 366–376.

14 B. Nakhjavan, M. N. Tahir, M. Panthöfer, H. Gao, T. Gasi, V. Ksenofontov, R. Branscheid, S. Weber, U. Kolb, L. M. Schreiber and W. Tremel, *Chem. Commun.*, 2011, **47**, 8898–8900.

15 S. H. Choi, B. N. Hyon, I. P. Yong, K. An, G. K. Soon, Y. Jang, M. H. Park, J. Moon, S. S. Jae, C. S. In, K. M. Woo and T. Hyeon, *J. Am. Chem. Soc.*, 2008, **130**, 15573–15580.

16 W. C. Smith, J. R. Morse, C. R. M. Bria, R. E. Schaak and S. K. R. Williams, *ACS Appl. Nano Mater.*, 2018, **1**, 6435–6443.

17 E. Fantechi, A. G. Roca, B. Sepúlveda, P. Torruella, S. Estradé, F. Peiró, E. Coy, S. Jurga, N. G. Bastús, J. Nogués and V. Puntes, *Chem. Mater.*, 2017, **29**, 4022–4035.

18 J. M. Hodges, J. R. Morse, M. E. Williams and R. E. Schaak, *J. Am. Chem. Soc.*, 2015, **137**, 15493–15500.

19 J. Graciani, K. Mudiyanselage, F. Xu, A. E. Baber, J. Evans, S. D. Senanayake, D. J. Stacchiola, P. Liu, J. Hrbek, J. Fernández Sanz and J. A. Rodriguez, *Science*, 2015, **345**, 546–550.

20 Y. Wang, Z. Chen, P. Han, Y. Du, Z. Gu, X. Xu and G. Zheng, *ACS Catal.*, 2018, **8**, 7113–7119.

21 M. Strach, V. Mantella, J. R. Pankhurst, P. Iyengar, A. Loiudice, S. Das, C. Corminboeuf, W. van Beek and R. Buonsanti, *J. Am. Chem. Soc.*, 2019, **141**, 16312–16322.

22 W. Shi, H. Zeng, Y. Sahoo, T. Y. Ohulchanskyy, Y. Ding, Z. L. Wang, M. Swihart and P. N. Prasad, *Nano Lett.*, 2006, **6**, 875–881.

23 C. Wang, W. Tian, Y. Ding, Y. Q. Ma, Z. L. Wang, N. M. Markovic, V. R. Stamenkovic, H. Daimon and S. Sun, *J. Am. Chem. Soc.*, 2010, **132**, 6524–6529.

24 H. Yu, M. Chen, P. M. Rice, S. X. Wang, R. L. White and S. Sun, *Nano Lett.*, 2005, **5**, 379–382.

25 Y. Wei, R. Klajn, A. O. Pinchuk and B. A. Grzybowski, *Small*, 2008, **4**, 1635–1639.

26 A. Heuer-Jungemann, N. Feliu, I. Bakaimi, M. Hamaly, A. Alkilany, I. Chakraborty, A. Masood, M. F. Casula, A. Kostopoulou, E. Oh, K. Susumu, M. H. Stewart, I. L. Medintz, E. Stratakis, W. J. Parak and A. G. Kanaras, *Chem. Rev.*, 2019, **119**, 4819–4880.

27 J. M. Hartley, C. M. Ip, G. C. H. Forrest, K. Singh, S. J. Gurman, K. S. Ryder, A. P. Abbott and G. Frisch, *Inorg. Chem.*, 2014, **53**, 6280–6288.

28 P. De Vreese, N. R. Brooks, K. Van Hecke, L. Van Meervelt, E. Matthijs, K. Binnemans and R. Van Deun, *Inorg. Chem.*, 2012, **51**, 4972–4981.

29 C. M. Gabardo, A. Seifitokaldani, J. P. Edwards, C.-T. Dinh, T. Burdyny, M. G. Kibria, C. P. O'Brien, E. H. Sargent and D. Sinton, *Energy Environ. Sci.*, 2018, **11**, 2531–2539.

30 Y. X. Chen, A. Miki, S. Ye, H. Sakai and M. Osawa, *J. Am. Chem. Soc.*, 2003, **125**, 3680–3681.

31 K. Larmier, W. C. Liao, S. Tada, E. Lam, R. Verel, A. Bansode, A. Urakawa, A. Comas-Vives and C. Copéret, *Angew. Chem., Int. Ed.*, 2017, **56**, 2318–2323.

32 D. Ren, J. Gao, L. Pan, Z. Wang, J. Luo, S. M. Zakeeruddin, A. Hagfeldt and M. Grätzel, *Angew. Chem., Int. Ed.*, 2019, **58**, 15036–15040.

33 Y. Xiong and Y. Xia, *Adv. Mater.*, 2007, **19**, 3385–3391.

34 Y. Yin and A. Paul, *Nature*, 2005, **437**, 664–670.

35 P. Rai, R. Khan, S. Raj, S. M. Majhi, K. K. Park, Y. T. Yu, I. H. Lee and P. K. Sekhar, *Nanoscale*, 2014, **6**, 581–588.

36 S. Narayanan, B. N. Sathy, U. Mony, M. Koyakutty, S. V. Nair and D. Menon, *ACS Appl. Mater. Interfaces*, 2012, **4**, 251–260.

37 X. Liu, J. Iocozzia, Y. Wang, X. Cui, Y. Chen, S. Zhao, Z. Li and Z. Lin, *Energy Environ. Sci.*, 2017, **10**, 402–434.